ELSEVIER

Chemical Geology 229 (2006) 78–95

CHEMICAL GEOLOGY
INCLUDING
ISOTOPE GEOSCIENCE

www.elsevier.com/locate/chemgeo

The compositional dependence of the saturation surface of H_2O+CO_2 fluids in silicate melts

Paolo Papale [a,b,*], Roberto Moretti [a,c], David Barbato [a,b]

[a] *Istituto Nazionale di Geofisica e Vulcanologia, Italy*
[b] *Sezione di Pisa, Via della Faggiola 32, 56126 Pisa, Italy*
[c] *Sezione Osservatorio Vesuviano, Via Diocleziano 328, 80124, Napoli*

Accepted 6 January 2006

Abstract

The volatile saturation surface in H_2O–CO_2–silicate melt systems is modeled by applying thermodynamic equilibrium between gaseous and liquid volatile components. The whole database of existing saturation data in the C–O–H–silicate liquid systems has allowed us to re-calibrate a previously developed fully multicomponent H_2O–CO_2 saturation model [Papale, P., 1999. Modeling of the solubility of a two-component H_2O+CO_2 fluid in silicate liquid. Am. Mineral., 84, 477–492]. The new database nearly doubles the previous one, greatly improving the performances of the whole model, which now adopts a significantly lower number of model parameters with respect to the previous calibration. The multicomponent H_2O+CO_2 saturation model is fully non-ideal, the only assumption being that the excess Gibbs free energy of the silicate mixture can be represented by an expansion of first-order symmetric interaction terms. No a-priori assumption is made on the P–T dependence of the volatile–oxide interaction terms, meaning that no assumption is made on the partial molar volume and enthalpy of the dissolved volatiles. The whole treatment is evaluated by restrictive statistical algorithms, which confirm the model validity on an extended database. The model allows to investigate extensively the dependence of the complex volatile saturation surface on composition. In order to explore the non-linear behaviors implicit in the physics of the dissolution process, the model is employed in a series of calculations aimed at illustrating some of the compositional features of the volatile saturation surface in both one-component and two-component volatile conditions. The results show compositional-dependent minima and maxima, some of which are known from the experiments. Non-ideal behavior is enhanced in two-component fluid phase conditions and pressures above a few hundreds MPa, where calculated isobaric H_2O–CO_2 saturation curves reveal the possible existence of a maximum in CO_2 saturation at non-zero H_2O contents. Due to the compositional dependence of the volatile saturation surface, it is outlined the important role played by redox conditions, especially in iron-rich melt systems like basalts.

Keywords: Multicomponent melts; Water solubility; Carbon dioxide solubility; Mixed volatile saturation; Thermodynamic modelling

1. Introduction

The knowledge of the saturation surface of multi-component fluids in silicate melts is long recognised to be a fundamental pre-requisite in industrial as well as geophysical problems and applications. Especially when dealing with natural magmas, a crucial role is played by

* Corresponding author. Istituto Nazionale di Geofisica e Vulcanologia, Sezione di Pisa, Via della Faggiola, 32, 56126 Pisa, Italy. Tel.: +39 050 8311931, (office); fax: +30 050 8311942.
E-mail address: papale@pi.ingv.it (P. Papale).

0009-2541/$ - see front matter © 2006 Elsevier B.V. All rights reserved.
doi:10.1016/j.chemgeo.2006.01.013

the composition of the liquid or melt in which volatile components can be dissolved. Indeed, natural magmas can display a huge variety of compositions, implying profound differences in the shape and position of the volatile saturation surface. A magma body, which rises through the Earth mantle and crust, is far from keeping its composition constant; on the contrary, it undergoes chemical reactions and differentiation, which deeply modify its bulk and liquid composition, determining a continuous shift in the equilibrium conditions between the liquid and gas (or supercritical) phases. In turn, the dissolved volatiles, especially water, determine a shift in the position of the liquidus and in the crystallization sequences, so that liquid–gas–crystal equilibria are mutually and deeply interrelated. Therefore, volatile concentrations in the liquid, and the corresponding composition and abundance of the gas phase in magma, continuously change along the cooling and differentiation history of magma, as a result of volatile concentration in the differentiated magma bodies and changes in the composition of the magmatic liquid. Additional compositional factors, which contribute to determine changes of the saturation surface, include mixing between different magma bodies, assimilation of country rocks and open system degassing.

Two different approaches can be found in the literature to model the saturation surface of volatiles in magmatic liquids. The first one is concerned with calibration of specific sets of data, often referred to a restricted compositional range and based on semi-empirical fitting procedures. This is for example the case of models proposed by Wasserburg (1957), Burnham and Davis (1971), Spera (1974), Eggler and Burnham (1984), Silver and Stolper (1985, 1989), Silver et al. (1990), Blank et al. (1993), Dixon et al. (1995), Dixon (1997), Zhang (1999) and Liu et al. (2005). Limited compositional variations can be accommodated in the model of Dixon (1997) for alkali-basalt from oceanic islands, by adopting linear relationships between SiO_2 and H_2O or CO_2. This first kind of approach guarantees a high reproducibility of experimental data in the P–T–X domain of interest, but does not allow reliable extrapolation to different conditions.

The second approach is more comprehensive, as it tries to model volatile saturation as a function of liquid components. In their pioneering work, Burnham and Nekvasil (1986) extended a previous work by Burnham and Davis (1971) and Burnham (1975, 1979), and calculated water solubility in silicate liquids through the computation of a compositionally dependent Henry's law analog quantity. Ghiorso et al. (1983), Ghiorso and Sack (1994) and Papale (1997, 1999) adopted a Margules-type formalism in which the thermodynamic properties of the liquid–gas mixture are modeled through binary interaction coefficients expressing the attractive-repulsive behavior of each pair of component molecules in magma. A similar approach was earlier followed by Nicholls (1980), although in this case the interactions regarded only the dissolved water and a general "melt" component (e.g., basalt, rhyolite, etc.).

In general, with the exception of the extended Burnham model, models of the second kind can be defined as thermodynamic per se, i.e., based on the computation of the Gibbs free energy of mixing and then able to provide component activities through the Gibbs–Duhem rule. Most of these models do not account for volatile speciation, which is not strictly required by thermodynamics itself. Although this implies less information with respect to structure-based models (e.g., Silver and Stolper, 1989), this choice largely simplifies the treatment of large databases, requiring thermodynamic theories of general validity in which the selected components (e.g., metal oxides) do not necessarily reflect the actual complexity and the structural changes of silicate melts upon volatile dissolution.

Multicomponent saturation models involving the contemporaneous presence of H_2O and CO_2 in the system were developed mainly as an extension of the above single-volatile models. Holloway and Blank (1994), Dixon (1997) and Newman and Lowenstern (2002) adopted the approach of Silver and Stolper (1985, 1989) to model H_2O+CO_2 saturation in basaltic and rhyolitic liquids under the assumption of Henry's law behavior. By employing a fully non-ideal non-Henrian model, Papale (1999) showed that the Henrian assumption is an oversimplification at pressure larger than 100 MPa, implying significant errors in the use of dissolved H_2O–CO_2 pairs as barometric indicators. In general, large errors are possible whenever a saturation model calibrated on narrow compositional ranges is used out of its field of calibration. On the other hand, the use of a fully compositional-dependent model may result in less accurate predictions on specific compositions for which experimental data are available, but it allows following the effects of compositional differences and compositional changes accompanying the evolution of natural magmas.

In this work, we re-calibrate the H_2O–CO_2–silicate liquid equilibrium model in Papale (1999) by including in the regression database the saturation data produced after 1997 and discuss through some examples of calculations the role of non-ideal, compositional

dependencies of the H_2O+CO_2 saturation surface in silicate melts. It is shown that the updated model is able to reproduce with satisfactory agreement more than 1100 single-volatile and two-volatile experimental data over an extremely wide *P*–*T*-compositional range. This capability, together with the fully non-ideal thermodynamic treatment (synthetically reported in Appendix A), ensures a confident use of the model to predict the shape and position of the complex volatile saturation surface over a large spectrum of synthetic silicate melt compositions and natural magmas on Earth.

2. New database and model regression

The extended database employed in the new calibration includes the data reported in Papale (1997, Tables 3 and 4), with the addition of the new data set reported in Table 1. This implies an increase of more than 500 data points, nearly doubling the original database. Thanks to many new data on CO_2 saturation made during last years, the pre-1980 CO_2 solubility data that were treated separately in Papale (1999), have been now discarded from the database. These data are known to have been affected by systematic errors due to the analytical technique used at that time (Blank et al., 1993). Additionally, the H_2O+CO_2 saturation data have now been fully employed in the regression procedure. The compositional range covered by the database is synthetically illustrated in Figs. 1 and 2. Fig. 1 shows that the database is widespread over the entire natural spectrum of compositions, but with some clustering as well as some holes. Most data, especially those for water (crosses), fall in the field of rhyolitic liquids with a highly variable content of alkalies up to trachytic and shoshonitic terms. A second clustering is present in the field of basalts. In general, the silica content varies over a large range from about 37 to 85 wt.% and total alkalies from 0 to more than 20 wt.%. Intermediate compositions are present but mostly as scattered data points. CO_2 solubility data (circles) show a higher clustering to compositions which are extreme with respect to natural conditions. On the contrary, H_2O+CO_2 saturation data are mostly focused on natural basaltic or rhyolitic compositions, showing no data points at very low or very high alkali contents.

Fig. 2 shows the relative proportions of basic oxides $+Fe_2O_3$ and is complementary to the TAS diagram in Fig. 1. The data show two major clusters, one towards the alkali-rich members and the other towards Fe–Mg–Ca-rich compositions. Intermediate compositions are in general well represented, as well as compositions along the boundaries of the triangular plot.

One significant problem when dealing with multicomponent saturation modeling is the $FeO–Fe_2O_3$ partition in the experimental runs. A few authors (Pan et al., 1991; Moore et al., 1995a; Gaillard et al., 2001; Wilke, 2002; Gaillard et al., 2003; Botcharnikov et al., 2005a) have directly determined the ferric–ferrous iron in the quenched experimental glass, while in other cases this ratio could be derived from the reported experimental oxygen fugacity (Dixon et al., 1995; Métrich and Rutherford, 1998; Yamashita, 1999; Tamic et al., 2001; Behrens and Jantos, 2001; Behrens et al., 2001; Berndt et al., 2002; King and Holloway, 2002; Roach, 2005). In all other cases, only the FeO_{TOT} is given. In such cases, it has been assumed that the oxygen fugacity corresponds to that along the $H_2O–H_2$ equilibrium at experimental *P*–*T* conditions, corresponding to assuming a sufficiently large abundance of the fluid phase to buffer the Fe^{III}/Fe^{II} ratio, which has been re-calculated by applying the model of Ottonello et al. (2001) extended in Moretti (2005).

The adopted regression procedure is based on a robust estimate technique with automatic recognition and exclusion of outliers, described in detail in Papale (1999, Appendix A). The regression procedure allows selection of molecule components according to Ghiorso et al. (1983) or Ghiorso and Sack (1994). Post-processing evaluation of the probability of correlation and of the standard deviation associated with binary interaction coefficients involving each H_2O– or CO_2–metal oxide pair shows that (i) the quality of database reproduction increases when molecule components from Ghiorso et al. (1983) are adopted, and (ii) Ti and Mn oxides are not statistically significant in the database due to general low abundance, resulting in overfitting of the related coefficients. As a consequence, we have re-calibrated the binary interaction coefficients involving each volatile–metal oxide pair by neglecting the interactions involving Ti and Mn oxides, assigning them a neutral or purely dilution effect in the calculation of the activity coefficients of dissolved volatiles.

In order to reduce as much as possible the number of necessary model parameters, we have repeated many times the regression by assuming different *P*–*T* dependencies of the reference molar volume of dissolved CO_2. The results show that the best compromise between accuracy of data reproduction and minimization of model parameters is achieved by adopting the following expression:

$$v_{CO_2} = a_1 + a_2 T + a_3 P \quad (1)$$

Table 1
Compositions included in the updated database, besides those listed in Papale (1997)

Composition	Investigated volatile	P (GPa)	T (K)	No. of data	Reference
Synthetic metaluminous melts	H_2O	0.2	1273	11	Gaillard et al. (2003)
Synthetic metaluminous melts, synthetic rhyolite, peraluminous obsidian glass, peralkaline obsidian glass	H_2O	0.201–0.228	1200	33	Gaillard et al. (2001)
Qz–Ab–An system	H_2O	0.5	1123–1223	7	Wilke et al. (2002)
Peralkaline rhyolite, andesite, augite minette	H_2O	0.0496–0.1985	1223–1401	22	Moore et al. (1995a)
Rhyolite	H_2O	0.022–0.1	1123–1473	15	Yamashita (1999)
$SiO–Na_2O$, $SiO_2–K_2O$	H_2O	0.05–0.8	1073–1693	50	Behrens et al. (2001)
Augite minette, basaltic andesite, silicic phonolite, biotite trachyte, leucitite	H_2O	0.0655–0.1951	1273–1453	16	Moore et al. (1995b)
Augite minette, basaltic andesite, silicic phonolite, biotite trachyte, leucitite	H_2O	0.1848–0.3110	1273–1453	16	Moore et al. (1998)
Phonolites	H_2O	0.0191–0.15	1123–1246	19	Carroll and Blank (1997)
Basalts	H_2O	0.0505–0.5009	1473	9	Berndt et al. (2002)
Haplogranites	H_2O	0.1–0.3	1073–1223	12	Schmidt et al. (1999)
Hawaiitic basalt	H_2O	0.027–0.08	1318–1408	10	Métrich and Rutherford (1998)
Granitic melts	H_2O	0.05–0.5	1073	36	Behrens and Jantos (2001)
Ab–Or join	H_2O	0.2	1313	13	Romano et al. (1995)
Ab–Or join	H_2O	0.2	1313	40	Romano et al. (1996)
Total new H_2O data				**309**	
$NaAlSiO_4–NaAlSi_6O_{14}$	CO_2	1–3.5	1723–1973	29	Brooker et al. (1999)
$SiO_2–Na_2O–Al_2O_3$± CaO±MgO	CO_2	0.2–2.7	1448–1973	50	Brooker et al. (2001)
Haplo-phonolite	CO_2	1–2.5	1573–1823	24	Morizet et al. (2002)
Total new CO_2 data				**103**	
Icelandite	$H_2O–CO_2$	1	1673	8	Jakobsson (1997)
Rhyolite	$H_2O–CO_2$	0.2–0.5	1073–1373	38	Tamic et al. (2001)
Ferribasalt	$H_2O–CO_2$	0.2	1473	11	Botcharnikov et al. (2005a)
Basalt	$H_2O–CO_2$	0.5	1423	4	Freise (2004)
Andesite	$H_2O–CO_2$	1	1573	5	King and Holloway (2002)
Hawaiitic basalt and rhyolite	$H_2O–CO_2$	0.112–0.215	1403–1433	15	Paonita et al. (2000)
Trachyte	$H_2O–CO_2$	0.02–0.15	1273–1453	10	Roach (2005)
Alkali basalt	$H_2O–CO_2$	0.0201–0.098	1473	15	Dixon et al. (1995)
Total new $H_2O–CO_2$ data				**106**	

This form corresponds to a reduction by 7 of the number of model parameters with respect to the corresponding form adopted in Papale (1999, Eq. (10)). The full expression and calibration from Burnham and Davis (1971) of a 10-parameter polynomial for the reference molar volume of dissolved H_2O is instead adopted, as in Papale (1997, 1999).

The best-fitting P–T dependence of the binary interaction coefficients involving volatiles has been tested in a series of regressions, each time evaluating the quality of database reproducibility and the probability of correlation. The extended database confirms that the best compromise between minimizing the number of model parameters and maximizing the reproducibility of the database corresponds to the use of a constant value for the interaction coefficients involving water, and of a pressure-dependent form for those involving carbon dioxide:

$$w_{H_2Oi} = w^{(0)}_{H_2Oi};\ w_{CO_2i} = w^{(0)}_{CO_2i} + w^{(1)}_{CO_2i} \ln \frac{P}{P^0} \qquad (2)$$

with $P^0 = 0.1$ MPa. The inclusion of a mixed volatile interaction term (w_{H2OCO2}) does not result in appreciable improvement of database reproducibility. The total

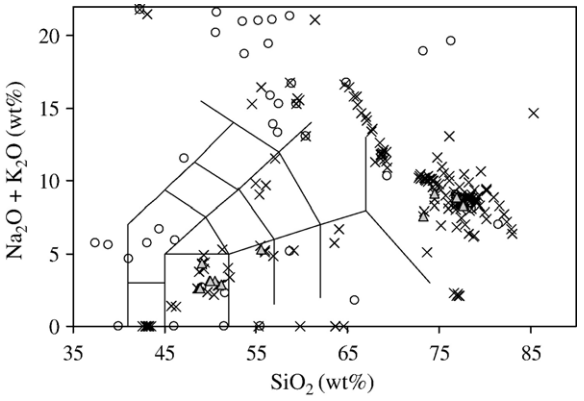

Fig. 1. TAS diagram showing the compositional distribution of data in the database for model regression. Crosses: data on H_2O solubility. Circles: data on CO_2 solubility. Triangles: data on H_2O+CO_2 saturation. Outliers (i.e. compositions automatically excluded by the robust regression procedure, see Papale, 1999, Appendix A) are not reported.

number of model parameters necessary to satisfactorily model about 1100 saturation data in the database is 29 (9 for H_2O and 20 for CO_2, Table 2), significantly less than the 42 model parameters previously employed (Papale, 1997, 1999) and corresponding to a model parameter/data ratio <0.026.

Table 2 reports the calibrated model parameters and standard deviations, while Fig. 3 shows a comparison with the Papale (1999) parameters. As it emerges from the figure, the addition of hundreds of new data on H_2O solubility and H_2O+CO_2 saturation, and the cancellation from the model parameters of the binary interaction coefficients involving TiO_2 and MnO, does not modify significantly the H_2O model parameters. This suggests that the H_2O-related model parameters are stable and that additional data from new H_2O solubility experiments in the future should not result in major changes in the model. On the contrary, the new CO_2 database results in significant changes of the CO_2-related model parameters, as a consequence of much poorer CO_2 database with respect to H_2O, and of major changes in the CO_2 database with respect to the one employed in previous work.

Fig. 4 shows the comparison between experimental and calculated solubility data for H_2O (a) and CO_2 (b), and between experimental and calculated pressure for H_2O+CO_2 saturation cases (c) (since the mixed volatile saturation surface depends on the total amount of H_2O and CO_2 in the system, the correspondence between experimental conditions and model calculations is more conveniently illustrated by comparing the experimental and calculated pressure, which is uniquely determined for each pair of dissolved volatiles). A total of 865 data on H_2O solubility, 173 data on CO_2 solubility and 84 data on H_2O+CO_2 saturation in silicate liquids is satisfactorily reproduced by the model. These data span pressure conditions from a few tens of MPa to a few GPa, temperature conditions from 800 to 2000 °C and volatile-free compositions from synthetic three-component oxide systems to natural silicate melts.

Fig. 5 shows the frequency distribution of the normalized error, or residuals, defined as the difference between calculated and experimental quantities divided by the calculated quantity. If the database is not affected by systematic errors and the model is not introducing some bias in the calculations, then the residuals must describe a Gaussian curve. Fig. 6 shows the results of a Kolmogorov–Smirnov (K–S) test (Chakravarti et al., 1967) made in order to evaluate whether the normalized error distributions are Gaussian. Such a test is therefore critical to evaluate whether the present model and database imply a random error distribution, which is inherent in any measurement and demanded for correct model calibration.

The test is based on the comparison between the cumulative distribution of the residuals and the cumulative normal distribution, or error function. The K–S statistical parameter D represents the maximum absolute vertical deviation between the two distributions and leads to the determination of the distribution probability P. A rule of thumb is that a value of P in the range 5–95% indicates that the two distributions do not differ significantly and that the test is satisfied (Press et al., 1992). The calculated values of P are 7.7%, 69.2% and 85.5% for H_2O, CO_2 and H_2O+CO_2, respectively (Fig. 6), demonstrating that the deviation of the normalized error distributions from Gaussian is within the confidence interval. The standard deviation of the

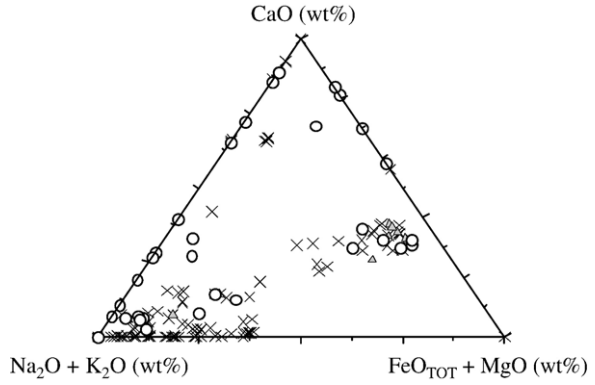

Fig. 2. Range of composition of data in the database for model calibration. Symbols as explained in the caption to Fig. 1. Outliers (i.e. compositions automatically excluded by the robust regression procedure, see Papale, 1999, Appendix A) are not reported.

Table 2
Calculated values of model parameters

Parameter	H_2O		CO_2	
	Calc. value	$\pm\sigma$	Calc. value	$\pm\sigma$
$w^{(0)}_{SiO_2\text{-volatile}}$	−34,093.073	631.624	−59,962.162	10,655.516
$w^{(0)}_{TiO_2\text{-volatile}}$ [a]	0		0	
$w^{(0)}_{Al_2O_3\text{-volatile}}$	−189,116.51	4801.53	−590,957.19	188,763.55
$w^{(0)}_{Fe_2O_3\text{-volatile}}$	135,935.31	12,675.48	4,469,622.8	389,809.7
$w^{(0)}_{FeO\text{-volatile}}$	−195,750.97	6130.38	21,665.755	174,650.472
$w^{(0)}_{MnO\text{-volatile}}$ [a]	0		0	
$w^{(0)}_{MgO\text{-volatile}}$	−86,418.051	6097.021	52,866.130	100,126.377
$w^{(0)}_{CaO\text{-volatile}}$	−209,996.65	3500.31	−328,792.10	75,671.61
$w^{(0)}_{Na_2O\text{-volatile}}$	−322,253.15	4581.66	140,034.45	204,101.93
$w^{(0)}_{K_2O\text{-volatile}}$	−349,797.50	6257.68	309,069.97	149,517.16
$w^{(1)}_{SiO_2\text{-volatile}}$	–		6049.2083	1162.9840
$w^{(1)}_{TiO_2\text{-volatile}}$ [a]	–		0	
$w^{(1)}_{Al_2O_3\text{-volatile}}$	–		41,395.372	19,366.940
$w^{(1)}_{Fe_2O_3\text{-volatile}}$	–		−529,301.20	46,628.86
$w^{(1)}_{FeO\text{-volatile}}$	–		1213.7172	18,203.847
$w^{(1)}_{MnO\text{-volatile}}$ [a]	–		0	
$w^{(1)}_{MgO\text{-volatile}}$	–		−13,446.202	10,512.946
$w^{(1)}_{CaO\text{-volatile}}$	–		12,788.832	8091.964
$w^{(1)}_{Na_2O\text{-volatile}}$	–		−35,213.194	21,144.787
$w^{(1)}_{K_2O\text{-volatile}}$	–		−58,009.539	15,940.154
$f^{\circ L}(P,T)$	19.793479	0.010017	23.484475	0.109585
a_1 in V_{CO_2}	[b]		2.41895E−06	1.57008E−06
a_2 in V_{CO_2}	[b]		1.34487E−08	6.43248E−10
a_3 in V_{CO_2}	[b]		2.10655E−15	1.39917E−15
P^0 (MPa) [a] (Eq. (2))	–	0.1		

[a] Not calibrated.
[b] Values of $a_{i=1,\ldots,10}$ terms for the molar volume of water have been taken from Burnham and Davis (1971).

normalized error distribution is 0.131 for water and 0.228 for carbon dioxide. For the experiments with mixed H_2O+CO_2 conditions, the standard deviation in the calculation of the saturation pressure is 0.096.

Fig. 7 shows the results of a two-distribution K–S test applied to check whether the experimental and calculated data series in Fig. 4 describe the same distribution within a statistically acceptable significance level. In this case, the cumulative distributions being compared correspond to the calculated and experimental H_2O solubility (Fig. 7a), CO_2 solubility (Fig. 7b) and H_2O+CO_2 saturation pressure (Fig. 7c). It is worth noting that the use of the K–S statistics in such a case becomes less robust, since the two calculated and experimental distributions loose their one-to-one correspondence, and since the distribution of the calculated values rests on least squares minimization over the experimental measurements with which it is compared. Nonetheless, such a K–S test is useful to show that the model matches the complex distribution patterns of saturation conditions for beyond 1100 data spanning huge ranges of P–T-composition conditions, as shown by the close correspondence of the calculated and experimental cumulative distributions and P values satisfying the test (Fig. 7).

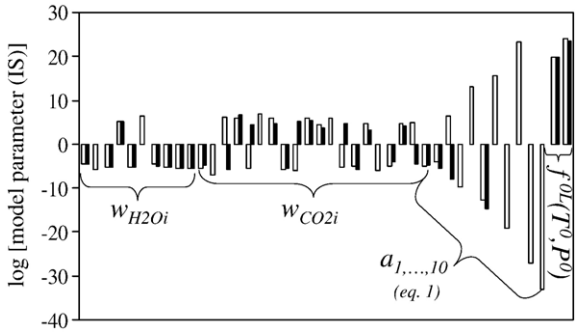

Fig. 3. Comparison between the present model parameter calibration (filled rods) and that in Papale (1999) (open rods). The sequence from left to right corresponds to that in Table 2, with the addition of previous model parameters for TiO_2 and MnO and of seven additional a parameters for the reference molar volume of dissolved CO_2 in Eq. (1), neglected in this work.

3. Model applications

The multicomponent volatile saturation model calibrated above is applied to a number of cases with the purpose of illustrating the role of non-ideal, compo-

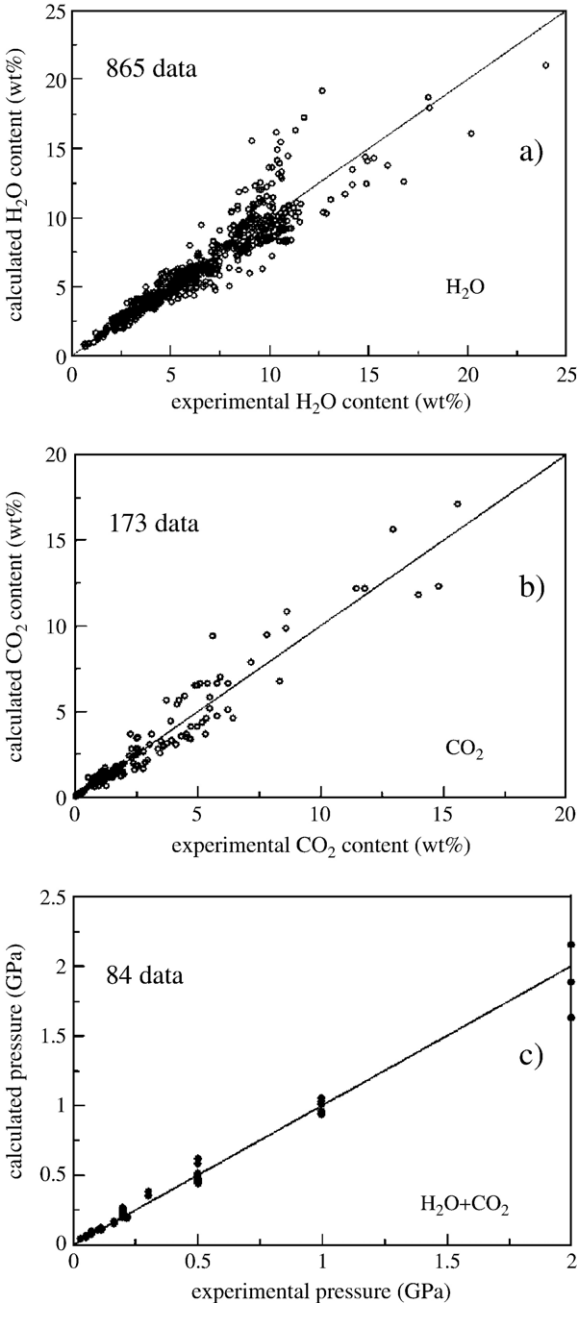

Fig. 4. Comparison between experimental and calculated H_2O solubility (a), CO_2 solubility (b) and H_2O+CO_2 saturation pressure (c). Outliers (i.e. compositions automatically excluded by the robust regression procedure, see Papale, 1999, Appendix A) are not reported.

sitional dependencies of the H_2O–CO_2 saturation surface in silicate melts. Selected cases correspond to the feldspar ternary, the Ab–An–Di system, the petrogeny's residua system and the mixing between different magmas. The results of additional calculations aimed at showing non-linear, non-ideal relationships arising in the system H_2O+CO_2+silicate melt at increasing pressure are also shown.

3.1. Feldspar ternary + H_2O

Fig. 8 shows the computed solubility of water in the system Ab–An–Kf, at the pressure of 200 MPa and temperature of 1673 K. Several features, part of which known from the experiments, emerge from the figure. The Ab–Kf join shows what has been called the *alkali effect* (Holtz et al., 1995; Romano et al., 1996), or the

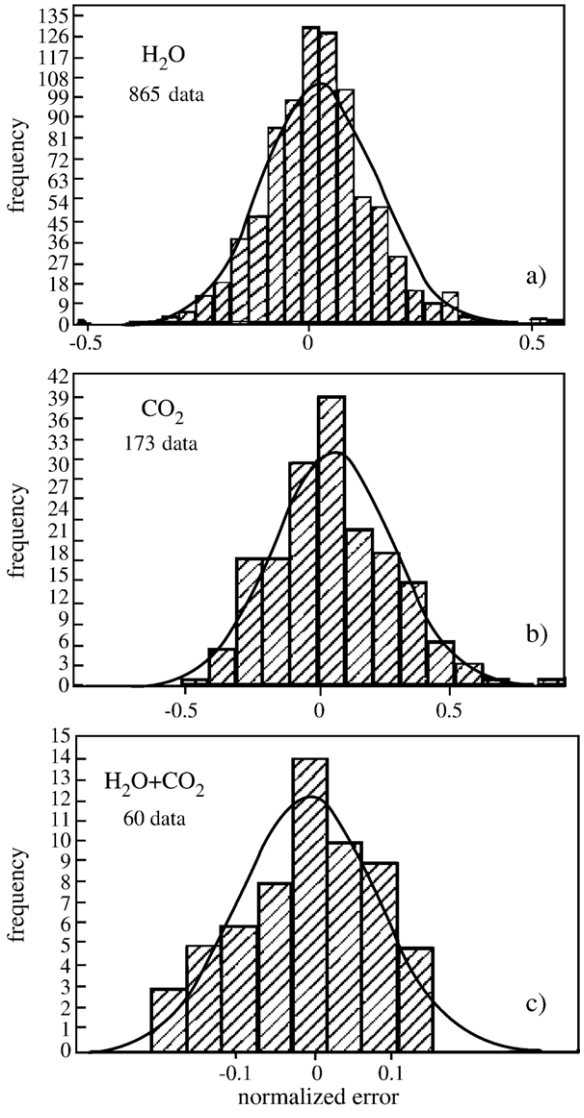

Fig. 5. Frequency distribution of the normalized error (difference between experimental and calculated value, normalized to calculated). (a) Water solubility, (b) carbon dioxide solubility, (c) H_2O+CO_2 saturation pressure. The number of classes is selected as roughly equal to the square root of the total number of samples.

progressive decrease of H_2O solubility with increasing K_2O content. The Ab–An join shows a solubility minimum, described in Paillat (1992) (although the experimental minimum appears closer to the An end-member). The An–Kf join has not been investigated experimentally. The present model reveals the existence of an absolute minimum in the ternary system corresponding to about 75 mol% Kf along the An–Kf join. In general, the figure shows how the fully multi-component nature of the modeling allows computing water solubility as a continuous function over the entire considered compositional range.

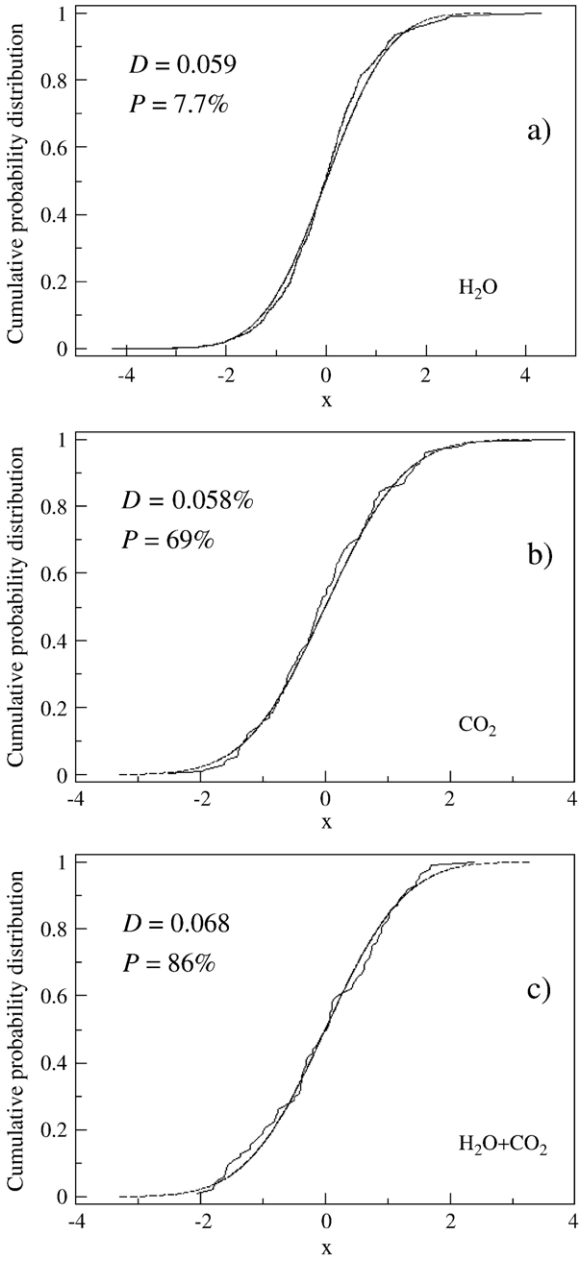

Fig. 6. Kolmogorov–Smirnov normality test on residuals for H_2O solubility (a), CO_2 solubility (b) and H_2O+CO_2 saturation pressure (c).

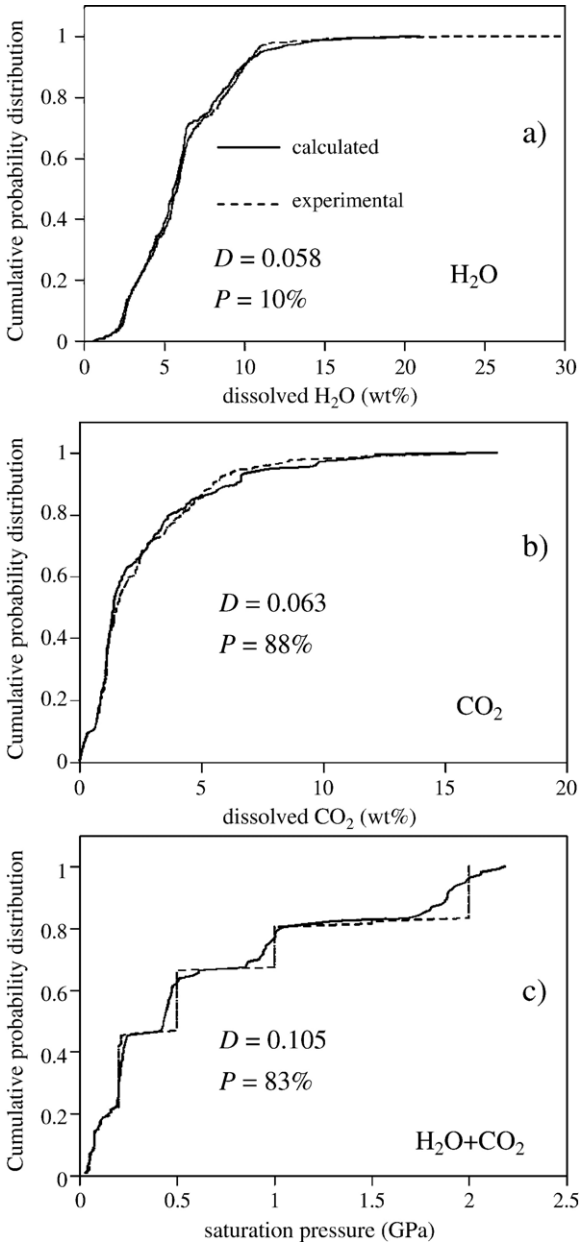

Fig. 7. Kolmogorov–Smirnov test for H_2O solubility (a), CO_2 solubility (c) and H_2O+CO_2 saturation (c). The step-like shape of the experimental curve in graph (c) is due to concentration of data at discrete pressure values.

3.2. Ab–An–Di system

Fig. 9 shows the H_2O and CO_2 solubility surface in the ternary Ab–An–Di system, at constant P–T of 100

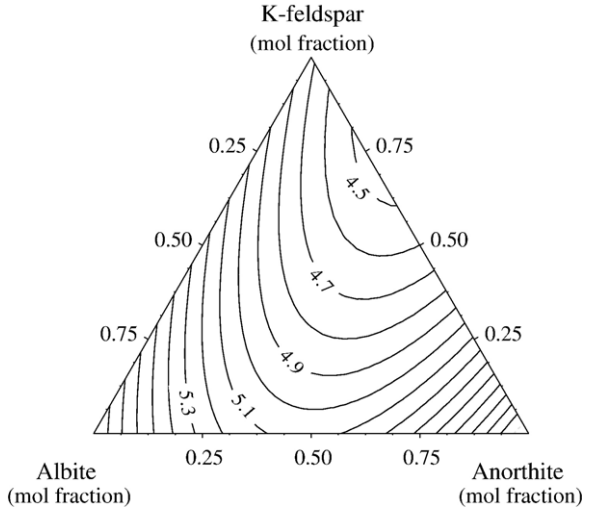

Fig. 8. Calculated shape of the H_2O solubility surface (wt.%) in the ternary feldspar system at $P=200$ MPa, $T=1673$ K, and neglecting liquid crystallization.

MPa and 1673 K. Water solubility shows three minima along the three binary joins, located roughly at 50 mol% composition and resulting in an absolute minimum at around $Ab_{38}An_{37}Di_{25}$. The three end-member compositions show similar water solubility of about 4 wt.% at the considered P–T conditions.

Carbon dioxide solubility shows instead a maximum value around 3.6 wt.% corresponding to the An end-member, progressively decreasing toward Di (3800 ppm) and Ab (700 ppm).

3.3. Petrogeny's residua system

Fig. 10 shows the H_2O solubility surface in the system Q–Ne–Ks at a pressure of 100 MPa and two different temperatures of 1100 (a) and 1400 (b) K, and compares such surfaces with the petrogeny's residua system at the same pressure and H_2O-saturated conditions. H_2O solubility shows at both temperatures the existence of a valley roughly following the Kf–Ab thermal divide and a minimum located close to the Kf composition. Fig. 10c reports approximate examples of differentiation paths (arrows) from different starting compositions (numbered circles, also reported as big dots in panels a and b). For each of them, the calculated solubility curves in Fig. 10a,b allow an evaluation of the changes in water solubility with differentiation. It is worth noting that the petrogeny's residua system is a non-isothermal plot, while the solubility surfaces at Fig. 9a,b refer to isothermal conditions. However, it can be seen that apart from a limited increase in water solubility with decreasing temperature, a difference of 300 K at 100 MPa does not produce important changes in the water solubility surface. Compositions 1 to 5 in Fig. 10c fractionate and evolve towards local and absolute minima by approximately following the water solubility paths shown in Fig. 10a,b.

3.4. Mixing of different magmas

A common occurrence during magmatic processes is represented by the mixing of different magma types, each with given composition and temperature and carrying different volatile contents. Magma mixing implies chemical homogenization at the molecular scale, sometimes occurring over a relatively short timescale of the order of days or hours (Rutherford and Gardner, 2000), and the generation of a hybrid magma

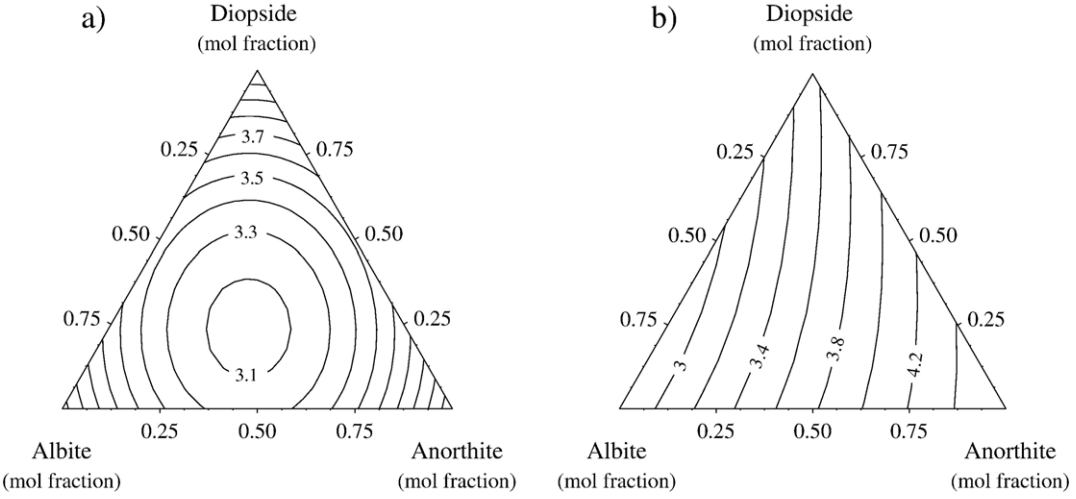

Fig. 9. Calculated shape of the (a) H_2O (wt.%) and (b) CO_2 ($\log_{10}$ [ppm]) solubility surface in the ternary system Ab–An–Di at $P=100$ MPa, $T=1673$ K, and neglecting liquid crystallization.

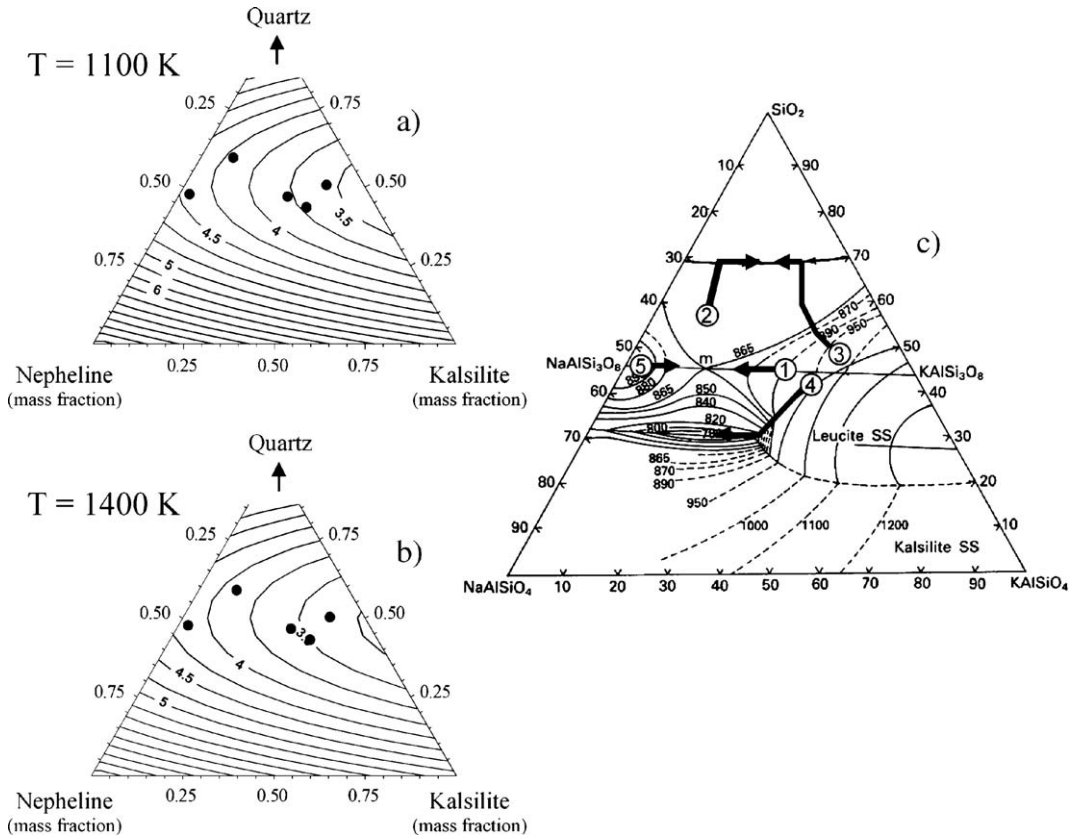

Fig. 10. Water solubility surface in the Q–Ks–Ne system at P=100 MPa and two different temperatures of (a) 1100 and (b) 1400 K, and (c) the petrogeny's residua system at same pressure and water saturated conditions (modified after D'Amico et al., 1987). The pure quartz end-member is not included in the solubility calculations since the present multicomponent model does not guarantee confident predictions for liquid compositions made of one single oxide. A few examples of possible liquid evolution paths from points 1–5 (also reported as dots in panels a and b) are reported in panel (c).

with intermediate composition and changed physico-chemical properties which result from the attainment of a new chemical equilibrium state (Russell, 1990). In such cases, it is necessary to dispose of a method to determine the new volatile saturation surface resulting from the new liquid composition and new volatile content.

Fig. 11 shows one such exercise. In this case three different magmatic liquids with rhyolitic, dacitic and basaltic melt composition are assumed to be characterized by pre-mixing conditions as reported in Table 3. The calculations reported in the figure refer to post-mixing equilibrium conditions, with the simplifying assumption of no crystallization. This is taken for simplicity, although crystallization can be included in principle. Post-mixing temperatures are roughly estimated by modeling the specific heats as in Ghiorso et al. (1983) on an anhydrous basis. The calculations are repeated for two different pressures of 100 and 400 MPa.

Fig. 11a shows a triangular plot of calculated temperatures as a function of the proportion of original magmas involved in the mixing. Since in the model of Ghiorso et al. (1983) the liquid specific heat is a linear function of temperature-independent partial molar contributions, the post-mixing temperature is a linear function of the proportion of each magma involved in the mixing.

Fig. 11b-i show the calculated post-mixing H_2O saturation surface, CO_2 saturation surface, gas phase composition and gas phase volume fraction, respectively. In multicomponent fluid phase conditions, the equilibrium varies with the total amount of each volatile component in the system. Therefore, each calculated point in the panels above shows the combined effect of local liquid-free composition, temperature and total H_2O–CO_2 in the system.

One of the most relevant features emerging from Fig. 11 is the way post-mixing quantities relate non-linearly with pressure. In fact, the 100 MPa calculations indicate

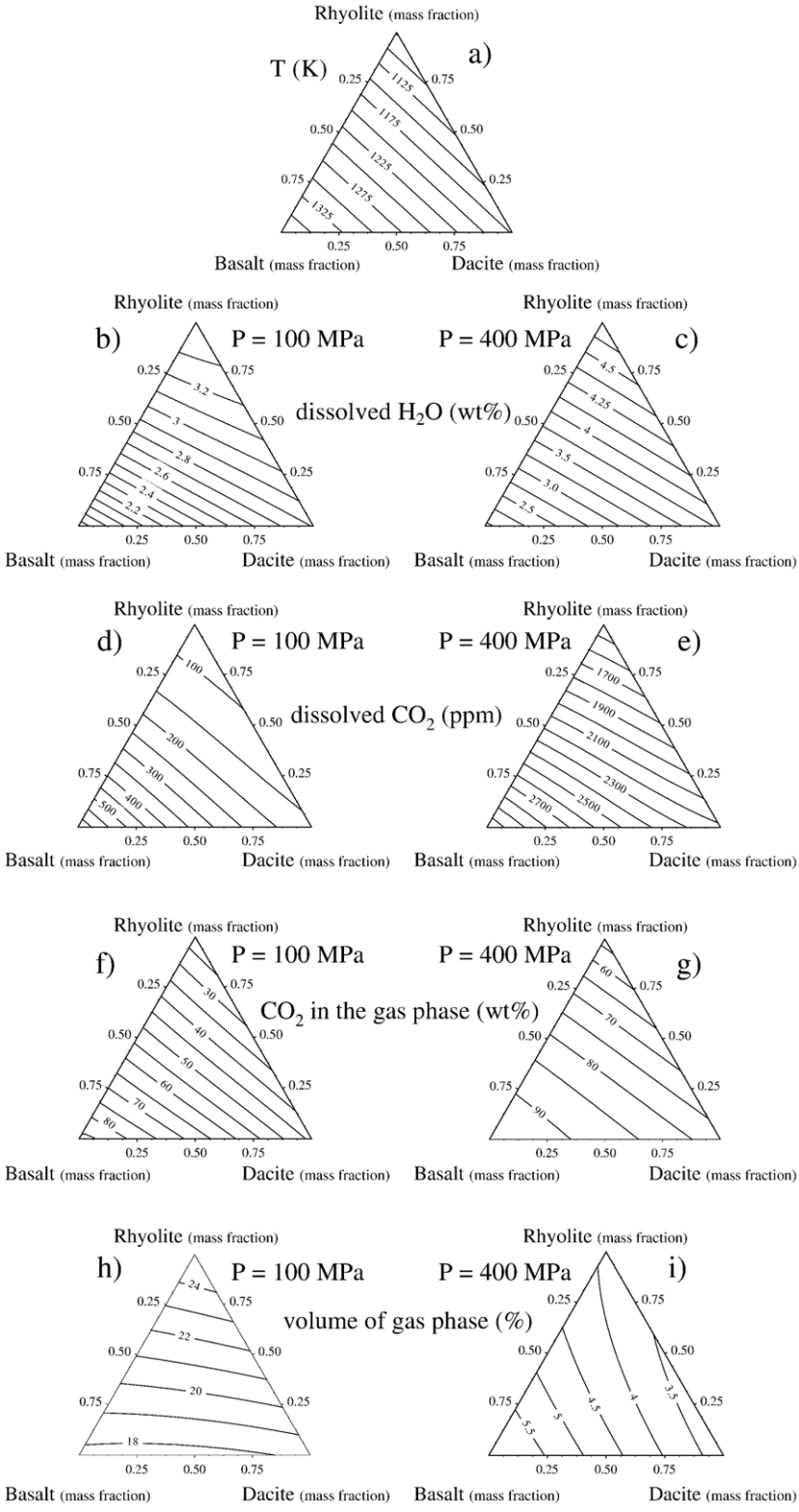

Fig. 11. Multicomponent liquid–gas equilibrium in the system rhyolite–dacite–basalt (composition, temperature and total volatile content of end-members in Table 3). Isolines constituted by equally spaced straight lines in panel (a) show the linear dependence of temperature on end-member proportions deriving from the model of Ghiorso et al. (1983).

Table 3
Volatile-free compositions (wt.%), total volatile contents (wt.%) and temperatures (K) adopted for the calculations in Fig. 11

Comp.	SiO_2	TiO_2	Al_2O_3	Fe_2O_3	FeO	MnO	MgO	CaO	Na_2O	K_2O	$w^T_{H_2O}$	$w^T_{CO_2}$	T
Basalt	50.26	1.22	17.18	1	7.88	0.15	6.80	10.16	3.56	0.93	2	2	1373
Dacite	66.57	0.56	15.92	1.70	1.82	0.08	1.51	4.16	4.11	2.24	4	1	1173
Rhyolite	72.49	0.24	14.06	0.9	0.77	0.07	0.72	2.06	4.21	3.26	6	0.8	1073

H_2O and CO_2 saturation as more markedly non-linearly related with mass of components, with respect to gas composition and volume. Instead, the 400 MPa case shows nearly linear dependence of H_2O and CO_2 saturation contents with component mass fraction and most evident non-linear dependence of gas composition. In the considered two-component fluid case, at both 100 and 400 MPa pressure, H_2O saturation content decreases from rhyolite to dacite to basalt, whereas CO_2 saturation content increases in the opposite direction. The most striking pressure-related non-linear effect concerns the volume of gas phase at equilibrium (Fig. 11h,i). Indeed, mixing at 100 MPa results in gas volume increasing from basalt to dacite to rhyolite, while mixing at 400 MPa results in an increasing trend from dacite to rhyolite to basalt. This means that, as a relevant example, mixing of a basaltic with a rhyolitic liquid under the conditions of the calculations in Fig. 11 will produce a mixed magma with gas volume fraction lower or larger than the initial value in the rhyolitic liquid, depending on pressure.

3.5. Non-ideal, non-linear $H_2O + CO_2$ interaction

The calibrated multicomponent $H_2O + CO_2$ saturation model is fully non-ideal, the only true assumption being that the excess Gibbs free energy of the silicate mixture can be represented by an expansion of first-order symmetric interaction terms (Ghiorso et al., 1983; Ghiorso and Sack, 1994; Papale, 1997, 1999). No a-priori assumption is made on the P–T dependence of the volatile–oxide interaction terms, meaning that no assumption is made on the partial molar volume and enthalpy of the dissolved volatiles. Rather, the best form is statistically evaluated a-posteriori on the basis of the correspondence between the experimental and calculated database (Papale, 1999, Appendix A).

Similarly, no a-priori assumption is made on H_2O–CO_2 interaction in the liquid. The statistics simply say that such a term is irrelevant for database reproducibility; therefore, it is a-posteriori set to zero. However, having this interaction being zero does not mean having no H_2O–CO_2 interaction in the liquid. As a matter of fact, the fully non-ideal formulation implies that the activity coefficient of each dissolved volatile largely depends on the other one, even if direct interaction is unimportant (Eqs. (A6) and (A7)). This is because the presence of each dissolved volatile effectively constitutes a modification of the chemical environment surrounding the other one. The effects of this mutual influence become large with increasing amount of dissolved volatiles, therefore, for a given volatile-free composition, with increasing pressure. The calculations show that non-ideal effects can be relevant at pressures above only 100 MPa (Fig. 11 in Papale, 1999).

Fig. 12 shows two examples referring to rhyolitic and basaltic compositions (reported in Holloway and Blank, 1994; Nuccio and Paonita, 2000, respectively). The calculations show the isobaric equilibrium concentrations of H_2O and CO_2 in the liquid, for two temperatures 300 K apart. The most interesting features for the present aim, emerging from the figure, are located in the proximity of the "dissolved CO_2" axis. Both the high-pressure rhyolitic and basaltic curves show in this region a significant deviation from the simpler low-pressure trends. In the rhyolitic case, such a deviation consists in the increase, rather than decrease, of the CO_2 saturation content when more H_2O is dissolved at constant pressure and temperature. This feature was first shown from experiments in pre-1980 papers by Mysen (1976) and Mysen et al. (1976), then again observed by Jakobsson (1997), King and Holloway (2002) and more extensively investigated in recent times by Botcharnikov et al. (2005b).

In the basaltic case in Fig. 12b, non-ideality close to the CO_2 axis takes the opposite sign and the high-pressure dissolved CO_2 shows a more rapid initial decrease, rather than an increase, with increasing amount of dissolved H_2O.

In neither case in Fig. 12, the calculated saturation curves show similar deviations in proximity of the H_2O axis. This can be easily understood by considering that dissolved H_2O contents are commonly 1 to 2 orders of magnitude larger than dissolved CO_2 contents; therefore, H_2O efficiency in determining an effective compositional change of the liquid with respect to CO_2 is much higher than the reverse.

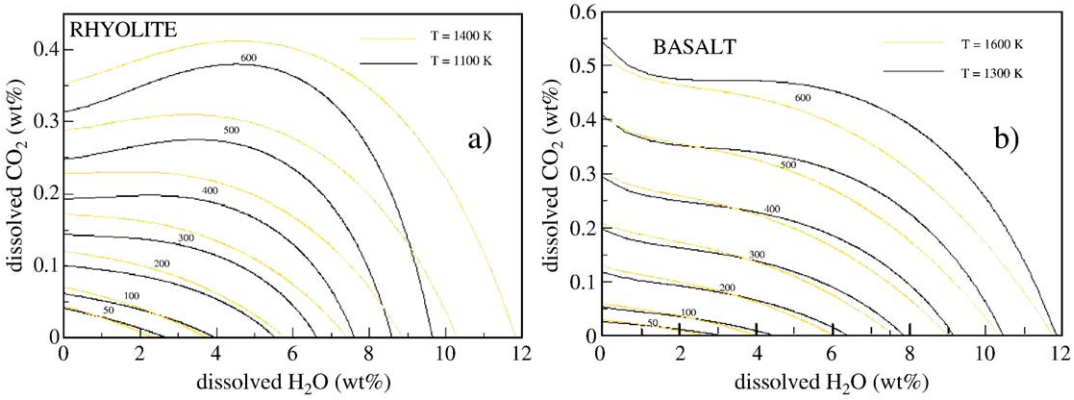

Fig. 12. Calculated equilibrium isobaric H_2O–CO_2 dissolved pairs in liquids of rhyolitic (a) and basaltic (b) compositions, each at two different temperatures. Numbers are pressure in MPa. Compositions from Holloway and Blank (1994) and Nuccio and Paonita (2000).

Other relevant elements emerging from Fig. 12 include the change from retrograde to prograde H_2O solubility in the rhyolitic liquid with increasing pressure, a feature well known from the experiments on albitic (Paillat et al., 1992) as well as rhyolitic (Yamashita, 1999) liquids. This same feature does not emerge from the calculations made with the basaltic liquid, for which H_2O solubility is found to decrease from 1300 to 1600 K temperature at any considered pressure (Fig. 12b). Differently, CO_2 solubility in the rhyolite shows prograde behavior at any pressure (Fig. 12a) and a change from prograde to retrograde with increasing pressure in the basalt (Fig. 12b). In general, for both compositions, the effect of temperature on H_2O+CO_2 saturation becomes larger with increasing pressure.

4. Discussion and conclusions

In this paper, we have made use of the whole database of existing saturation data in the C–O–H–silicate liquid system in order to re-calibrate a previously developed fully multicomponent, non-ideal H_2O–CO_2 saturation model. The number of new data, the extension of the compositional conditions in the experiments and the increased accuracy of the determinations made during last years make the new database a tough test for the model, and give a chance to remove from the calibration the pre-1980 CO_2 saturation data, which show a general poor consistency with the determinations made during last 25 years.

Model calibration does not only include the determination of best numbers for unknown quantities in the model; rather, it means in this case also defining the best P–T dependency of model parameters. This is done by comparing statistic quantities related to different assumed dependencies and taking as the best model the one with the greatest score.

Actually, volatile saturation data alone are not suited to define such dependencies. In principle, activity coefficients of volatile components and volatile saturation data bring about information on P–T terms in the contribution of volatiles to the excess Gibbs free energy of the liquid, hence on the binary interaction terms involving volatiles. However, it is the joined consideration of saturation, volume and enthalpy data, which is required for drawing full information on the excess Gibbs free energy G^E of volatile-bearing liquids. Volume data should be used to constrain the P terms in G^E, enthalpy data to constrain the non-linear T terms and saturation data to constrain everything including the linear T terms and the P–T independent terms. In this way, an internally consistent, general thermodynamic model for volatile–silicate liquid interaction could be obtained.

Unfortunately, volume and enthalpy data of volatile-bearing silicate melts are very scarce, significantly below the number requested for multicomponent regression, forcing us to employ saturation data only. This produces P–T dependencies and numbers, which are functional for their specific objective of reproducing saturation data, but the true P–T dependence of G^E is not necessarily well approximated. As an example, the P–T-independent form of the H_2O-related binary interaction coefficients determined in this work (first of Eq. (2)) implies a composition-independent partial molar volume of H_2O dissolved in silicate melts (and a slightly compositional-dependent partial molar volume in the presence of carbon dioxide), but this does not mean that such a quantity is really composition-independent. Rather, it simply means that in order to reproduce the H_2O database there is

no advantage from considering that dependence. Similarly, the *P*-dependent interaction coefficients involving CO_2 tell us that the inclusion of compositional-dependent partial molar volume of dissolved CO_2 results in an effective improvement of the model capability to reproduce the database within the adequate statistical constraints. It can be appreciated that this improvement may relate to the strong compositional dependence of the CO_2 speciation on melt composition, compared with the less strong dependence of H_2O speciation on melt composition (e.g., Botcharnikov et al., 2006-this issue).

With the same logics, the logarithmic dependence of the $w_{CO_2}i$ parameters on *P* at the second term of Eq. (2) simply represents an efficient form for reproducing saturation data and not necessarily contains the real *P* dependence of the excess Gibbs free energy. In fact, the partial molar volume of dissolved CO_2 descending from Eq. (2) has an hyperbolic shape when plotted against pressure, producing either extremely high or extremely low values at atmospheric pressure. This does not affect the calculation of saturation conditions, since the relevance of the *P* term in Eq. (2) only appears at pressure much higher than atmospheric, but tells us clearly that we are still far from a general thermodynamic model of volatile–silicate melt interaction and that such a model cannot be produced if a comprehensive database of volume and enthalpy data for volatile-bearing silicate melts is not available.

Although the statistics are satisfactory for both H_2O and CO_2 solubility, we note that (i) the huge difference between H_2O and CO_2 databases inevitably results in much more confident calculations for the former, and (ii) this brings about an increased uncertainty in the calculations of H_2O+CO_2 saturation. The fact that no important variations of H_2O-related model parameters emerges when nearly doubling the number of data in the database (Fig. 3) is a further confirmation that H_2O solubility in silicate melts of virtually any composition can be satisfactorily predicted by the present model. On the contrary, the large changes in CO_2-related model parameters calibrated in Papale (1999) and in this work reflect the much more controversial nature of the corresponding database. Due to this and to much lower data/parameter ratio (17.1 for CO_2 and 114.8 data per parameter for H_2O, since each H_2O+CO_2 saturation datum produces two rows in the regression matrix, both containing H_2O- and CO_2-related model parameters), it is expected that the future production of a much more exhaustive database for CO_2 may result in a significant improvement of model accuracy.

An additional element adding uncertainty to model predictions on iron-rich melt compositions, especially those involving CO_2, comes from the relatively few data for which the experimental oxygen fugacity is reported. As said above, in all cases where no fO_2 estimate was available, we have used the polymeric model of Ottonello et al. (2001) and its extension to hydrous conditions (Moretti, 2005). In this model, iron oxidation state is modeled by considering that (i) FeO undergoes a basic dissociation in the Lux–Flood sense (Flood and Förland, 1947), producing Fe^{2+} and O^{2-} (i.e., free oxygens); (ii) Fe_2O_3 has an amphoteric behavior, i.e., trivalent iron may produce both Fe^{3+} cations (basic dissociation in the Lux–Flood sense) and FeO_2^- anions (acidic dissociation in the Lux–Flood sense); (iii) water is treated as an amphoteric oxide dissociating in OH^- and H^+, consistently with NMR results of Xue and Kanzaki (2004), and exerting a chemical role on the ferric to ferrous iron ratio. The calculated standard deviations for the calibrated binary interaction terms reported in Table 2 show maximum values for iron oxides, as a consequence of error summation deriving from the uncertain fO_2 conditions during data production and use of the iron speciation model in Moretti (2005) within the present calibration. Calculated H_2O and CO_2 solubilities in a variety of basaltic melts carrying from 8 to 12 wt.% iron (volatile-free) show a substantial dependence on the Fe_2O_3/FeO mass ratio. Changes of such a ratio from 0 to 1 produce a decrease by 5–25% of the H_2O solubility, this effect decreasing with increasing pressure from 100 to 500 MPa. For CO_2 at 100 MPa, the calculated solubility decrease turns out to be 80–90%, while at 500 MPa CO_2 solubility is found to increase by about a factor 2.

The above discussion suggests the following: (i) fO_2 conditions may be of great importance for volatile solubility, especially for CO_2, as a consequence of the control on iron speciation; (ii) control of the fO_2 conditions during the experiments should be ensured in order to increase the quality of the solubility data and the confidence of model calibration and predictions.

Some examples of calculations involving both synthetic and natural compositions are reported in this paper, and several features of the H_2O, CO_2 or H_2O+CO_2 saturation surface are outlined. For those cases involving natural compositions, it is worth taking in mind that none of the above features should be generalized as being representative of natural counterparts, e.g., generic "rhyolites" or "basalts". Natural compositions taking the same name in classic classification schemes can be significantly different, while both modeling and experiments are increasingly

revealing features related to non-ideal, non-linear roles of liquid composition in multicomponent gas–liquid equilibria. As a matter of fact, each composition, even if taking the same general name or falling within the same classificative box, should be separately investigated in the P–T range of interest, either experimentally or through multicomponent modeling. Only after a-posteriori evaluation of the results one may conclude that the compositional differences can be neglected, or they must be taken into account, in order to describe the complex shape of the volatile saturation surface and the many features of multicomponent gas–liquid equilibrium.

Acknowledgements

Mark Ghiorso and Bjorn O. Mysen are acknowledged for their constructive reviews. This work was partially funded by the Italian Dipartimento della Protezione Civile in the frame of the 2004–2006 Agreement with Istituto Nazionale di Geofisica e Vulcanologia-INGV (Projects V2 "Stromboli", V3_2 "Campi Flegrei" and V3_6 "Etna"). **[RR] [PR]**

Appendix A. Synthetic description of the thermodynamic model

The thermodynamic model which forms the basis of the present re-calibration is extensively described in previous papers (Papale, 1997, 1999). Here we include a synthetic description of its mathematics.

The basic mechanical, thermal and chemical equilibrium equations are the followings:

$$P^{\mathrm{G}} = P^{\mathrm{L}} = P$$

$$T^{\mathrm{G}} = T^{\mathrm{L}} = T$$

$$f^{\mathrm{G}}_{\mathrm{H_2O}} = f^{\mathrm{L}}_{\mathrm{H_2O}} \Rightarrow \phi_{\mathrm{H_2O}} y_{\mathrm{H_2O}} P = \gamma_{\mathrm{H_2O}} x_{\mathrm{H_2O}} f^{\mathrm{oL}}_{\mathrm{H_2O}}$$

$$f^{\mathrm{G}}_{\mathrm{CO_2}} = f^{\mathrm{L}}_{\mathrm{CO_2}} \Rightarrow \phi_{\mathrm{CO_2}} y_{\mathrm{CO_2}} P = \gamma_{\mathrm{CO_2}} x_{\mathrm{CO_2}} f^{\mathrm{oL}}_{\mathrm{CO_2}} \quad \text{(A1)}$$

where f is fugacity, ϕ is the fugacity coefficient in the gas phase, γ is the activity coefficient in the liquid phase, y and x are mole fractions in the gas and liquid phase, respectively, the superscripts G and L refer to the gas and liquid phase, respectively, and the superscript oL refers to the reference state in the liquid phase. These equations are closed by the mass balance equations

$$y_{\mathrm{H_2O}} + y_{\mathrm{CO_2}} = 1$$

$$\frac{x^{\mathrm{T}}_{\mathrm{H_2O}} - y_{\mathrm{H_2O}}}{y_{\mathrm{H_2O}} - x_{\mathrm{H_2O}}} = \frac{x^{\mathrm{T}}_{\mathrm{CO_2}} - y_{\mathrm{CO_2}}}{y_{\mathrm{CO_2}} - x_{\mathrm{CO_2}}} \quad \text{(A2)}$$

where the superscript T refers to total mole fractions, i.e., with respect to the gas–liquid mixture.

The fugacity coefficient in the gas phase is calculated by means of the equation of state by Kerrick and Jacobs (1981) for H_2O, CO_2 and H_2O–CO_2 mixtures. The reference state for volatiles dissolved in the liquid phase is obtained by standard thermodynamic relationships:

$$\ln f^{\mathrm{oL}}_i(P,T) = \ln f^{\mathrm{oL}}_i(P^{\mathrm{o}},T^{\mathrm{o}}) + \int_{P^{\mathrm{o}}}^{P} \frac{v^{\mathrm{o}}_i}{RT}\mathrm{d}P - \int_{T^{\mathrm{o}}}^{T} \frac{1}{RT^2} \int_{P^{\mathrm{o}}}^{P} \times \left[v^{\mathrm{o}}_i - T\left(\frac{\partial v^{\mathrm{o}}_i}{\partial T}\right)_P \right] \mathrm{d}P\mathrm{d}T \quad \text{(A3)}$$

where v is molar volume, R is the universal gas constant and the superscript o refers to a standard state defined at P^{o} and T^{o}.

The activity coefficient of volatiles dissolved in the liquid phase is calculated from an expression for the excess Gibbs free energy G^{E} through the following:

$$\left(\frac{\partial G^{\mathrm{E}}}{\partial n_i}\right)_{P,T,n_{j\neq i}} = RT\ln\gamma_i \quad \text{(A4)}$$

where n is the number of moles, and the subscripts i and j denote components. The general expression for G^{E} is analogous to that in Ghiorso et al. (1983), Ghiorso and Sack (1994) and similar papers:

$$G^{\mathrm{E}} = N \sum\nolimits_{i=1}^{n-1} \sum_{j=i+1}^{n} x_i x_j w_{ij} \quad \text{(A5)}$$

where N is the total number of moles, n is here the number of components and w_{ij} denotes Margules-type interaction coefficients between pairs of components. The interaction coefficients not involving volatiles are taken from Ghiorso et al. (1983), implying that the composition of the liquid phase is re-written in terms of 8-oxygen oxide components as in that paper. The resulting expressions for the activity coefficients of dissolved H_2O and CO_2 are the following:

$$\begin{aligned} RT\ln\gamma_{\mathrm{H_2O}} = {} & (1-x_{\mathrm{H_2O}})x_{\mathrm{CO_2}} w_{\mathrm{H_2OCO_2}} \\ & + (1-x_{\mathrm{H_2O}})(1-x_{\mathrm{H_2O}}-x_{\mathrm{CO_2}}) \\ & \times \sum_{i\neq \mathrm{CO_2}=1}^{n} x'_i w^{(0)}_{\mathrm{H_2O}i} - x_{\mathrm{CO_2}} \\ & \times (1-x_{\mathrm{H_2O}}-x_{\mathrm{CO_2}}) \left[\sum_{i\neq \mathrm{H_2O}=1}^{n} x'_i w^{(0)}_{\mathrm{CO_2}i} \right. \\ & \left. + \ln\frac{P}{P^{\mathrm{o}}} \sum_{i\neq \mathrm{H_2O}=1}^{n} x'_i w^{(1)}_{\mathrm{CO_2}i} \right] \\ & -(1-x_{\mathrm{H_2O}}-x_{\mathrm{CO_2}})^2 \\ & \times \sum_{i\neq \mathrm{H_2O,CO_2}=1}^{n-1} \sum_{j\neq \mathrm{H_2O,CO_2}=i+1}^{n} x'_i x'_j w_{ij} \end{aligned} \quad \text{(A6)}$$

$$RT\ln\gamma_{CO_2} = (1-x_{CO_2})x_{H_2O}w_{H_2OCO_2} - x_{H_2O}(1-x_{H_2O}-x_{CO_2}) \times \sum_{i\neq CO_2=1}^{n} x_i' w_{H_2Oi}^{(0)} + (1-x_{CO_2}) \times (1-x_{H_2O}-x_{CO_2}) \times \left[\sum_{i\neq H_2O=1}^{n} x_i' w_{CO_2 i}^{(0)} + \ln\frac{P}{P^o} \sum_{i\neq H_2O=1}^{n} x_i' w_{CO_2 i}^{(1)} \right] - (1-x_{H_2O}-x_{CO_2})^2 \times \sum_{i\neq H_2O,CO_2=1}^{n-1} \sum_{j\neq H_2O,CO_2=i+1}^{n} x_i' x_j' w_{ij} \quad (A7)$$

where x' denotes concentration of non-volatile components in the volatile-free liquid:

$$x_{i\neq H_2O,CO_2}' = \frac{x_i}{1-x_{H_2O}-x_{CO_2}} \quad (A8)$$

It is worth noting that the adoption of the Ghiorso et al. (1983) volatile-free interaction parameters, instead of the more recent Ghiorso and Sack (1994) parameters, does not allow direct use of the present H_2O–CO_2 saturation model into the MELTS code without loosing internal consistency demanded by the Gibbs–Duhem relation. As explained in the text, this choice follows the significantly better correspondence found between the database and model calculations when using the Ghiorso et al. (1983) parameters, while ensuring internal consistency of the present model per se. An operative coupling of the present model and MELTS should be however possible, similarly to the coupling between H_2O+CO_2 and S saturation models based on different expressions for the excess Gibbs free energy, as done in Moretti et al. (2003) and Moretti and Papale (2004).

References

Behrens, H., Jantos, N., 2001. The effect of anhydrous composition on water solubility in granitic melts. Am. Mineral. 86, 14–20.

Behrens, H., Meyer, M., Holta, F., Benne, D., Nowak, M., 2001. The effect of alkali ionic radius, temperature, and pressure on the solubility of water in $MAlSi_3O_8$ melts (M=Li, Na, K, Rb). Chem. Geol. 174, 275–289.

Berndt, J., Liebske, C., Holtz, F., Freise, M., Nowak, M., Ziegenbein, D., Hurkuk, W., Koepke, J., 2002. A combined rapid-quench and H_2-membrane setup for internally heated pressure vessels: description and application for water solubility in basaltic melts. Am. Mineral. 87, 1717–1720.

Blank, J.G., Stolper, E.M., Carroll, M.R., 1993. Solubilities of carbon dioxide and water in rhyolitic melts at 850 °C and 750 bars. Earth Planet. Sci. Lett. 119, 27–36.

Botcharnikov, R.E., Koepke, J., Holtz, F., McCammon, C., Wilke, M., 2005a. The effect of water activity on the oxidation and structural state of Fe in a ferro-basaltic melt. Geochim. Cosmochim. Acta. 69, 5071–5085.

Botcharnikov, R., Freise, H., Holtz, F., Behrens, H., 2005b. Solubility of C–O–H mixtures in natural melts: new experimental data and application range of recent models. Ann. Geophys. 48, 633–646.

Botcharnikov, R.E., Behrens, H., Holtz, F., 2006-this issue. Solubility and speciation of C–O–H fluid in andesitic melt at T=1100 −1300 °C and P=200 and 500 MPa. Chem. Geol. 229, 125–143 doi:10.1016/j.chemgeo.2006.01.016.

Brooker, R.A., Kohn, S.C., Holloway, J.R., McMillan, P.F., Carroll, M. R., 1999. Solubility, speciation and dissolution mechanisms for CO_2 in melts on the $NaAlO_2$–SiO_2 join. Geochim. Cosmochim. Acta 63, 3549–3566.

Brooker, R.A., Kohn, S.C., Holloway, J.R., McMillan, P.F., 2001. Structural controls on the solubility of CO_2 in silicate melts: Part I. Bulk solubility data. Chem. Geol. 174, 225–239.

Burnham, C.W., 1975. Water and magmas: a mixing model. Geochim. Cosmochim. Acta 39, 1077–1084.

Burnham, C.W., 1979. The importance of volatile constituents. The Evolution of Igneous Rocks. Princeton University Press, Princeton, NJ, pp. 1077–1084.

Burnham, C.W., Davis, N.F., 1971. The role of H_2O in ilicate melts: I. P–V–T relations in the system $NaAlSi_3O_8$–H_2O to 10 kilobars, 700 °C to 1100 °C. Am. J. Sci. 272, 902–940.

Burnham, C.W., Nekvasil, H., 1986. Equilibrium properties of granitic magmas. Am. Mineral. 71, 239–263.

Carroll, M.R., Blank, J.G., 1997. The solubility of H_2O in phonolitic melts. Am. Mineral. 82, 549–556.

Chakravarti, I.M., Laha, R.G., Roy, J., 1967. Handbook of Methods of Applied Statistics, vol. I. John Wiley and Sons.

D'Amico, C., Innocenti, F., Sassi, F.P., 1987. Magmatismo e Metamorfismo. UTET, Torino.

Dixon, J.E., 1997. Degassing of alkalic basalts. Am. Mineral. 82, 368–378.

Dixon, J.E., Stolper, E.M., Holloway, J.R., 1995. An experimental study of water and carbon dioxide solubilities in mid-ocean ridge basaltic liquids: Part I. Calibration and solubility models. J. Petrol. 36, 1607–1631.

Eggler, D.H., Burnham, C.W., 1984. Solution of H_2O in diopside melts: a thermodynamic model. Contrib. Mineral. Petrol. 85, 58–66.

Flood, H., Förland, T., 1947. The acidic and basic properties of oxides. Acta Chem. Scand. 1, 952–1005.

Freise, M., 2004. Differenzierung von Basalten einer "Large Igneous Province" am Beispiel des Kerguelen Plateaus. Eine experimentelle Studie. PhD thesis, University of Hannover.

Gaillard, F., Scaillet, B., Pichavant, M., Bény, J.-M., 2001. The effect of water and fO_2 on the ferric–ferrous ratio of silicic melts. Chem. Geol. 174, 255–273.

Gaillard, F., Pichavant, M., Scaillet, B., 2003. Experimental determination of activities of FeO and Fe_2O_3 components in hydrous silicic melts under oxidizing conditions. Geochim. Cosmochim. Acta 67, 4389–4409.

Ghiorso, M.S., Sack, R.O., 1994. Chemical mass transfer in magmatic processes: IV. A revised internally consistent thermodynamic model for the interpolation and extrapolation of liquid–solid equilibria in magmatic systems at elevated temperatures and pressures. Contrib. Mineral. Petrol. 119, 197–212.

Ghiorso, M.S., Carmichael, I.S.E., Rivers, M.L., Sack, R.O., 1983. The Gibbs free energy of mixing of natural silicate liquids; an expanded regular solution approximation for the calculation of magmatic intensive variables. Contrib. Mineral. Petrol. 84, 107–145.

Holloway, J.R., Blank, J.G., 1994. Application of experimental results to C–O–H species in natural melts. In: Carroll, M.R., Holloway, J. R. (Eds.), Volatiles in Magmas. Reviews in Mineralogy, vol. 30, pp. 187–230.

Holtz, F., Behrens, H., Dingwell, D.B., Johannes, W., 1995. H_2O solubility in haplogranitic melts: compositional, pressure, and temperature dependence. Am. Mineral. 80, 94–108.

Jakobsson, S., 1997. Solubility of water and carbon dioxide in an icelandite at 1400 °C and 10 kilobars. Contrib. Mineral. Petrol. 127, 129–135.

Kerrick, D.H., Jacobs, G.K., 1981. A modified Redlick-Kwong equation for H_2O, CO_2, and H_2O–CO_2 mixtures at elevated pressures and temperatures. Am. J. Sci. 281, 735–767.

King, P.L., Holloway, J.R., 2002. CO_2 solubility and speciation in intermediate (andesitic) melts: the role of H_2O and composition. Geochim. Cosmochim. Acta 66, 1627–1640.

Liu, Y., Zhang, Y., Behrens, H., 2005. Solubility of H_2O in rhyolitic melts at low pressures and a new empirical model for mixed H_2O +CO_2 solubility in rhyolitic melts. J. Volcanol. Geotherm. Res. 143, 219–235.

Métrich, N., Rutherford, M.J., 1998. Low pressure crystallization paths of H_2O-saturated basaltic-hawaiitic melts from Mt. Etna: implications for open-system degassing of basaltic volcanoes. Geochim. Cosmochim. Acta 62, 1195–1205.

Moore, G., Righter, K., Carmichael, I.S.E., 1995a. The effect of dissolved water on the oxidation state of iron in natural silicate liquids. Contrib. Mineral. Petrol. 120, 170–179.

Moore, G., Vennemann, T., Carmichael, I.S.E., 1995b. Solubility of water in magmas to 2 kbar. Geology 23, 1099–1102.

Moore, G., Vennemann, T., Carmichael, I.S.E., 1998. An empirical model for the solubility of H_2O in magmas to 3 kilobars. Am. Mineral. 83, 36–42.

Moretti, R., 2005. Polymerisation, basicity, oxidation state and their role in ionic modelling of silicate melts. Ann. Geophys. 48, 583–608.

Moretti, R., Papale, P., 2004. On the oxidation state and volatile behavior in multicomponent gas-melt equilibria. Chem. Geol. 213, 265–280.

Moretti, R., Papale, P., Ottonello, G., 2003. A model for the saturation of C–O–H–S fluids in silicate melts. In: Oppenheimer, C., Pyle, D.M., Berclay, J. (Eds.), Volcanic Degassing. Geol. Soc. London, Spec. Publ., vol. 213, pp. 81–101.

Morizet, Y., Brooker, R.A., Kohn, S.C., 2002. CO_2 in haplo-phonolite melt: solubility, speciation and carbonate complexation. Geochim. Cosmochim. Acta 66, 1809–1820.

Mysen, B.O., 1976. The role of volatiles in silicate melts: solubility of carbon dioxide and water in feldspars, pyroxene, and feldspathoid melts to 30 kb and 1625 °C. Am. J. Sci. 276, 969–996.

Mysen, B.O., Eggler, D.H., Seitz, M.G., Holloway, J.R., 1976. Carbon dioxide solubilities in silicate melts and crystals: Part I. Solubility measurements. Am. J. Sci. 276, 455–479.

Newman, S., Lowenstern, J.B., 2002. VolatileCalc: a silicate melt–H_2O–CO_2 solution model written in Visual Basic for Excel. Comput. Geosci. 28, 597–604.

Nicholls, J., 1980. A simple thermodynamic model for estimating the solubility of H_2O in magmas. Contrib. Mineral. Petrol. 74, 211–220.

Nuccio, P.M., Paonita, A., 2000. Investigation of the noble gas solubility in H_2O–CO_2 bearing silicate liquids at moderate pressure: II. The extended ionic porosity (EIP) model. Earth Planet. Sci. Lett. 183, 499–512.

Ottonello, G., Moretti, R., Marini, L., Vetuschi Zuccolini, M., 2001. On the oxidation state of iron in silicate melts and glasses: a thermochemical model. Chem. Geol. 174, 157–179.

Paillat, O., 1992. Structures et propriétés des liquides et verres silicatés feldspathiques hydratés. PhD thesis, Institut National Polytechnique de Lorraine, France.

Paillat, O., Elphick, S.C., Brown, W.L., 1992. The solubility of water in $NaAlSi_3O_8$ melts: a re-examination of Ab–H_2O phase relationships and critical behaviour at high pressures. Contrib. Mineral. Petrol. 112, 490–501.

Pan, V., Holloway, J.R., Hervig, R.L., 1991. The pressure and temperature dependence of carbon dioxide solubility in tholeiitic basalt melts. Geochim. Cosmochim. Acta 55, 1587–1595.

Paonita, A., Gigli, G., Gozzi, D., Nuccio, P.H., Trigila, R., 2000. Investigation of the He solubility in H_2O–CO_2 bearing silicate liquids at moderate pressure: a new experimental method. Earth Planet. Sci. Lett. 181, 595–604.

Papale, P., 1997. Thermodynamic modeling of the solubility of H_2O and CO_2 in silicate liquids. Contrib. Mineral. Petrol. 126, 237–251.

Papale, P., 1999. Modeling of the solubility of a two-component H_2O+CO_2 fluid in silicate liquid. Am. Mineral. 84, 477–492.

Press, W.H., Teukolsky, S.A., Vetterling, W.T., Flannery, B.P., 1992. Numerical Recipes in Fortran. Cambridge University Press. 963 pp.

Roach, A., 2005. The evolution of silicic magmatism in the post-caldera volcanism of the Phlegrean fields, Italy. PhD thesis, Brown University.

Romano, C., Dingwell, D.B., Behrens, H., 1995. The temperature dependence of the speciation of water in $NaAlSi_3O_8$–$KAlSi_3O_8$ melts: an application of fictive temperatures derived from synthetic fluid-inclusions. Contrib. Mineral. Petrol. 122, 1–10.

Romano, C., Dingwell, D.B., Behrens, H., Dolfi, D., 1996. Compositional dependence of water solubility along the joins $NaAlSi_3O_8$–$KAlSi_3O_8$, $NaAlSi_3O_8$–$LiAlSi_3O_8$ and $KAlSi_3O_8$–$LiAlSi_3O_8$. Am. Mineral. 81, 452–461.

Russell, J.K., 1990. Magma mixing processes: insights and constraints from thermodynamic calculations. Rev. Miner. 24, 153–190.

Rutherford, M.J., Gardner, J.E., 2000. Rates of magma ascent. In: Sigurdsson, H. (Ed.), Encyclopedia of Volcanoes. Academic Press, San Diego, pp. 207–217.

Schmidt, B.C., Holtz, F., Pichavant, M., 1999. Water solubility in haplogranitic melts coexisting with H_2O–H_2 fluids. Contrib. Mineral. Petrol. 136, 213–224.

Silver, L., Stolper, E., 1985. A thermodynamic model for hydrous silicate melts. J. Geol. 93, 161–178.

Silver, L., Stolper, E., 1989. Water in albitic glasses. J. Petrol. 30, 667–710.

Silver, L., Ihinger, P.D., Silver, L., 1990. The influence of bulk composition on the speciation of water in silicate glasses. Contrib. Mineral. Petrol. 104, 142–162.

Spera, F.J., 1974. A thermodynamic basis for predicting water solubilities in silicate melts and implications for the low velocity zone. Contrib. Mineral. Petrol. 45, 175–186.

Tamic, N., Behrens, H., Holtz, F., 2001. The solubility of H_2O and CO_2 in rhyolitic melts in equilibrium with a mixed CO_2–H_2O fluid phase. Chem. Geol. 174, 333–347.

Wasserburg, G.J., 1957. The effects of H_2O in silicate systems. J. Geol. 65, 15–23.

Wilke, M., Behrens, H., Burkhard, D.M.J., Rossano, S., 2002. The oxidation state of iron in silicic melt at 500 MPa water pressure. Chem. Geol. 189, 55–67.

Xue, X., Kanzaki, M., 2004. Dissolution mechanisms of water in depolymerized silicate melts: constraints from ^{1}H and ^{29}Si NMR spectroscopy and ab initio calculations. Geochim. Cosmochim. Acta 68, 5027–5057.

Yamashita, S., 1999. Experimental study of the effect of temperature on water solubility in natural rhyolite melt to 100 MPa. J. Petrol. 40, 1497–1507.

Zhang, Y., 1999. H_2O in rhyolitic glasses and melts: measurement, speciation, solubility, and diffusion. Rev. Geophys. 37, 493–516.